
This is an electronic reprint of the original article.
This reprint may differ from the original in pagination and typographic detail.

Karhunen, J.; Carr, M.; Harrison, J. R.; Lomanowski, B.; Balboa, I.; Carvalho, P.; Groth, M.; Huber, A.; Matthews, G. F.; Meakins, A.; Silburn, S.

Effect of reflections on 2D tomographic reconstructions of filtered cameras and on interpreting spectroscopic measurements in the JET ITER-like wall divertor

Published in:
Review of Scientific Instruments

DOI:
[10.1063/1.5118885](https://doi.org/10.1063/1.5118885)

Published: 01/10/2019

Document Version
Publisher's PDF, also known as Version of record

Please cite the original version:
Karhunen, J., Carr, M., Harrison, J. R., Lomanowski, B., Balboa, I., Carvalho, P., Groth, M., Huber, A., Matthews, G. F., Meakins, A., & Silburn, S. (2019). Effect of reflections on 2D tomographic reconstructions of filtered cameras and on interpreting spectroscopic measurements in the JET ITER-like wall divertor. *Review of Scientific Instruments*, 90(10), 1-11. Article 103504. <https://doi.org/10.1063/1.5118885>

This material is protected by copyright and other intellectual property rights, and duplication or sale of all or part of any of the repository collections is not permitted, except that material may be duplicated by you for your research use or educational purposes in electronic or print form. You must obtain permission for any other use. Electronic or print copies may not be offered, whether for sale or otherwise to anyone who is not an authorised user.

Effect of reflections on 2D tomographic reconstructions of filtered cameras and on interpreting spectroscopic measurements in the JET ITER-like wall divertor

Cite as: Rev. Sci. Instrum. **90**, 103504 (2019); <https://doi.org/10.1063/1.5118885>

Submitted: 05 July 2019 . Accepted: 19 September 2019 . Published Online: 14 October 2019

J. Karhunen, M. Carr , J. R. Harrison, B. Lomanowski, I. Balboa, P. Carvalho, M. Groth , A. Huber, G. F. Matthews, A. Meakins, S. Silburn, and JET Contributors



View Online



Export Citation



CrossMark

ARTICLES YOU MAY BE INTERESTED IN

[An edge fast-ion D-alpha system installed at ASDEX Upgrade](#)

Review of Scientific Instruments **90**, 103501 (2019); <https://doi.org/10.1063/1.5121588>

[A newly designed actively water-cooled Langmuir probe for tokamak devices](#)

Review of Scientific Instruments **90**, 103503 (2019); <https://doi.org/10.1063/1.5113636>

[Insulation improvement of an all-solid pulse forming line with film dielectric](#)

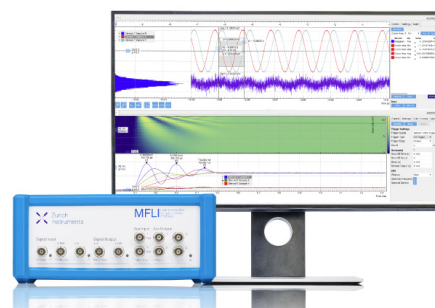
Review of Scientific Instruments **90**, 104705 (2019); <https://doi.org/10.1063/1.5115178>

Challenge us.

What are your needs for periodic signal detection?



Zurich
Instruments



Effect of reflections on 2D tomographic reconstructions of filtered cameras and on interpreting spectroscopic measurements in the JET ITER-like wall divertor

Cite as: Rev. Sci. Instrum. 90, 103504 (2019); doi: 10.1063/1.5118885

Submitted: 5 July 2019 • Accepted: 19 September 2019 •

Published Online: 14 October 2019



View Online



Export Citation



CrossMark

J. Karhunen,^{1,a)} M. Carr,² J. R. Harrison,² B. Lomanowski,³ I. Balboa,² P. Carvalho,⁴ M. Groth,¹ A. Huber,⁵ G. F. Matthews,² A. Meakins,² S. Silburn,² and JET Contributors^{b)}

AFFILIATIONS

¹Aalto University, Department of Applied Physics, 02150 Espoo, Finland

²CCFE, Culham Science Centre, Abingdon OX14 3DB, United Kingdom

³Oak Ridge National Laboratory, Oak Ridge, Tennessee 37831, USA

⁴Instituto de Plasmas e Fusão Nuclear, Instituto Superior Técnico, 1049-001 Lisboa, Portugal

⁵Institut für Energie- und Klimaforschung – Plasmaphysik, Forschungszentrum Jülich, 52425 Jülich, Germany

^{a)}juuso.karhunen@aalto.fi

^{b)}See the author list of “Overview of the JET preparation for Deuterium-Tritium Operation” by Joffrin *et al.* to be published in Nuclear Fusion Special Issue: Overview and Summary Reports from the 27th Fusion Energy Conference (Ahmedabad, India, 22–27 October 2018).

ABSTRACT

Considering reflections from metallic wall surfaces in generation of tomographic reconstructions of the tangentially viewing, visible-range spectroscopic divertor cameras in JET has been observed to yield enhanced spatial accuracy and significant reduction of emission artifacts in experimentally resolved 2D line emission distributions. Neglect of reflections in the tomography process was found to lead to overestimation of the emission near the wall surfaces by up to a factor of 4, as well as to formation of bright emission artifacts between the main emission regions and the wall surfaces, comprising locally up to 50% of the emission. Mimicking divertor spectroscopy measurements by integrating the tomographic reconstructions along vertical lines-of-sight implies that reflections comprise 15%–25% of the observed line-integrated emission peaks. The spatial differences in the reflection contribution between the different lines-of-sight are less pronounced than in the 2D reconstructions due to the dominance of the brightest emission regions through which the spectroscopic lines-of-sight pass. However, post-processing EDGE2D-EIRENE simulations using the CHERAB code and synthetic spectroscopy suggests a decrease of the spectroscopically inferred divertor electron temperature by up to 75%, when redistribution of the observed light due to reflections is considered.

Published under license by AIP Publishing. <https://doi.org/10.1063/1.5118885>

I. INTRODUCTION

Radiation of plasma fuel and impurities in the divertor volume has an important role in divertor detachment and power exhaust to avoid damage of plasma-facing components.^{1–3} Moreover, spectroscopic measurements of the divertor emission allow inference of electron density (n_e) and temperature (T_e) in the divertor.^{4–6} In

JET, in addition to bolometric measurements of total radiation,⁷ divertor emission is observed with vertical spectroscopic lines-of-sight,^{8–10} as well as with a visible-range spectroscopic divertor camera system (KL11).¹¹ The divertor camera setup consists of four cameras equipped with a selection of changeable narrow band-pass filters with bandwidths of 1–3 nm for visible-range emission of hydrogen isotopes and various impurity species, viewing the

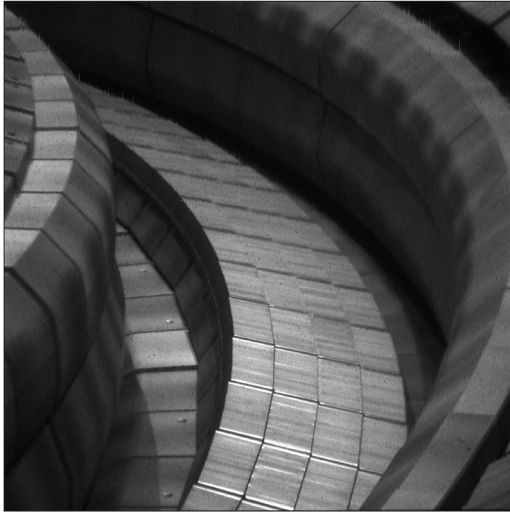


FIG. 1. The KL11 camera system observes the JET divertor tangentially. Image courtesy of G. Arnoux.

divertor tangentially, as shown in Fig. 1. The cameras are calibrated using the in-vessel calibration light source (ICLS) setup of JET,^{12–14} providing reference data for spectroscopic analysis in absolute units of intensity.

Tomographic reconstructions of tangential camera views are an established method for resolving the 2D distribution of divertor emission in various tokamak devices,^{15–23} including the spectroscopic divertor camera system in JET.^{24,25} The reconstructed 2D emission distributions assist in localizing the line-integrated divertor spectroscopy measurements, allow inferring, e.g., the spatial evolution of ionization and recombination fronts, and provide valuable reference data for divertor plasma modeling. However, especially in the case of all-metallic wall configurations, such as the ITER-like wall of JET,²⁶ camera measurements can be affected by reflections from the wall surfaces. Blending of the emitted and reflected light complicates the interpretation of the divertor emission, which can distort the tomographic reconstructions, as has previously been observed in the ASDEX Upgrade²² and COMPASS²³ tokamaks with reflective tungsten and stainless steel wall configurations, respectively. In both cases, addressing the reflections in the tomography process was found to improve the reconstructions through removal of background emission artifacts.

In this work, the new improved reflection correction presented by Carr *et al.*²⁷ is applied on tomographic reconstructions of spectroscopic camera images in the tungsten divertor of JET. The effect of reflections on the tomography solutions is resolved by comparing the reflection-corrected reconstructions to uncorrected ones. The contribution of reflections in line-integrated spectroscopy signal is investigated by synthesizing divertor spectroscopy measurements across the tomographic reconstructions. In addition, the effect of reflection-induced redistribution of observed light on spectroscopic measurements of divertor plasma parameters is studied by postprocessing solutions of EDGE2D-EIRENE^{28–30} simulations.

II. REFLECTION-CORRECTED TOMOGRAPHY

Assuming toroidally symmetric plasma emission, the intensity of every pixel i of the camera image, p , can be considered as a weighted sum of every cell j in the 2D emission distribution, f , according to

$$p_i = \sum_j W_{ij} f_j. \quad (1)$$

The connection between the 2D distribution, comprised of N_{cells} grid cells, and the camera image with N_{pixels} pixels is given by the $N_{\text{pixels}} \times N_{\text{cells}}$ -sized geometry matrix, W , whose elements describe the weights of each distribution cell, f_j , on each image pixel, p_i . The weights are given by the geometry of the camera view and primarily set by the path lengths of the poloidal projections of the camera sight lines, corresponding to each camera pixel, within each cell of the 2D reconstruction grid. In the presence of reflections, this is, however, not a sufficient description for the connection between f and p , as the pixels record also reflected emission, whose origin does not lie along the corresponding sight lines. As a result, the reflected light is interpreted as plasma emission, which decreases the accuracy of tomographic reconstructions.

As a new feature for divertor camera tomography in JET, utilizing ray-tracing and a model for surface reflectivity and roughness has further allowed resolving the contribution of every f_j on the camera image for a given view also via reflections, as fully described in Ref. 27. This is illustrated by the synthetic camera image in Fig. 2(a), providing a camera view of plasma emission in a single cell in the 2D emission distribution, whose location above the horizontal outer target is marked with purple crosses in Figs. 2(b) and 2(c). The bright red stripe in the image is produced by the emitting cell, while the rest of the image is comprised of reflections of this emission from the wall surfaces, in this case reaching up to 20% of the intensity of the plasma emission itself. The additional contributions due to reflections have been integrated into the geometry matrix, which increases the emphasis of the cells near wall surfaces, as shown by the normalized total weights of the 2D distribution cells, summed over all image pixels, in Fig. 2(c). Reflections are, thus, made part of the geometry definition of the tomography process, which improves the representativity of Eq. (1) in describing the connection between the 2D plasma emission distribution and the camera image. Consequently, the tomographic reconstructions present only the plasma emission without misinterpreted reflected light, improving their capability of representing the divertor plasma conditions, as well as their comparability to simulations.

Material-specific reflectivity and roughness properties have been optimized for beryllium and tungsten, respectively, and applied to all surfaces of the aforementioned materials across the first wall.²⁷ This, however, does not take spatial differences in the reflection properties—arising, e.g., due to plasma-wall interactions—into account. Since the inner divertor is characterized by formation of co-deposited layers, while the outer divertor is more prominently a net-erosion zone,³¹ the surface structure and reflection properties are expected to deviate between the tungsten components on opposite sides of the divertor. Moreover, to allow use of a single geometry matrix for all camera filters, averages of the wavelength-dependent reflectivities over the visible wavelength range have been

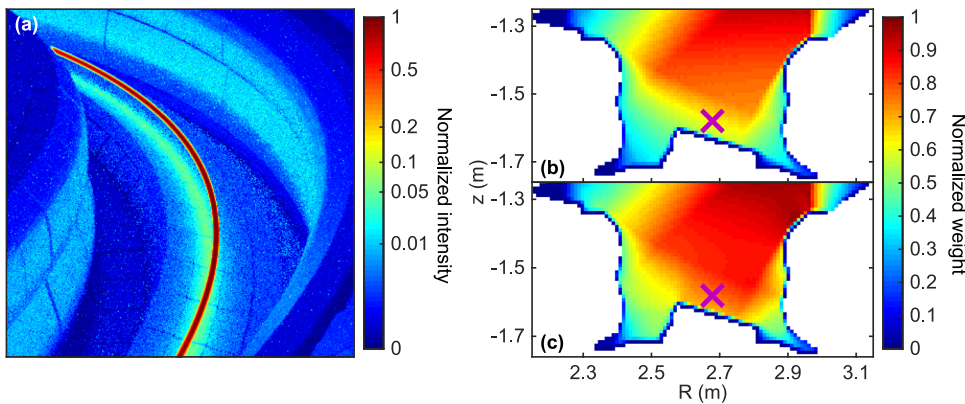


FIG. 2. Ray-tracing allows resolving the contribution of each emission distribution cell in each camera image pixel due to camera viewing geometry and reflections (a). The image in (a) correspond to the emission in a single cell marked with a purple cross in (b) and (c). The introduction of reflections increases the weight of the cells near wall surfaces (c) with respect to a geometry matrix without the reflection contributions (b). Note the nonlinear color bar in (a).

used in defining the reflection properties. To investigate the significance and eliminate the averaging effects arising from the use of single material-specific and wavelength-averaged reflection properties, spatial variation of surface roughness and reflectivity, as well as wavelength dependence of the latter, will be considered in further development of the model.

Using the reflection-corrected geometry matrix, the 2D emission distribution, f , is solved iteratively from Eq. (1) using the Simultaneous Adaptive Algebraic Reconstruction Technique (SAART)

$$f_j^{k+1} = f_j^k + \frac{\lambda}{\sum_i W_{ij}} \sum_i \left[\frac{W_{ij} f_j^k}{\sum_j W_{ij} f_j^k} \left(p_i^{\text{cam}} - \sum_i W_{ij} f_j^k \right) \right], \quad (2)$$

where k is the iteration round, λ is a constant relaxation parameter, and p_i^{cam} is the i th pixel of the camera image. The SAART algorithm is a modification of the established Simultaneous Algebraic Reconstruction Technique (SART),³² utilizing an adaptive method, presented in Ref. 33, of weighing the correction term, $p_i^{\text{cam}} - \sum_i W_{ij} f_j^k$, in Eq. (2). The latter emphasizes the contribution of emission in cell j in pixel i of the synthetic camera image by applying the weighing factor $\frac{W_{ij} f_j^k}{\sum_j W_{ij} f_j^k}$, while SART weighs the cells strictly according

to the camera viewing geometry by $\frac{W_{ij}}{\sum_j W_{ij}}$. This modification was

observed to improve the localization of the emission in the tomographic reconstructions by reducing the smoothing of the emission along the camera sight lines.

The tomographic reconstructions are generated on a 2D grid, restricted by the JET wall contour, with 2992 rectangular cells of $1.0 \text{ cm} \times 1.0 \text{ cm}$ in the divertor volume, as presented in Fig. 3(a). This cell size provides a sufficiently high resolution to resolve the spatial features of the emission distributions without excessively reducing the computation speed of the solution. Since the camera view is not strictly tangential but observes the divertor at a vertical angle from above, the grid extends upward from the divertor to approximately 0.5 m below the midplane to the origin of the camera field-of-view. While the tomographic reconstructions are not trusted outside the divertor due to restricted camera view, extending the grid outside the divertor to cover the entire field-of-view provides a space for the reconstruction algorithm to deposit the emission observed between

camera endoscope and the divertor, which decreases background halos in the divertor in the reconstructions. To decrease the effect of the extended grid on the computation speed, larger grid cells of $3.0 \text{ cm} \times 3.0 \text{ cm}$ are used in the main chamber. In both the divertor and the main chamber, cells outside the camera view are excluded in the tomography process, as indicated by the green and red colors

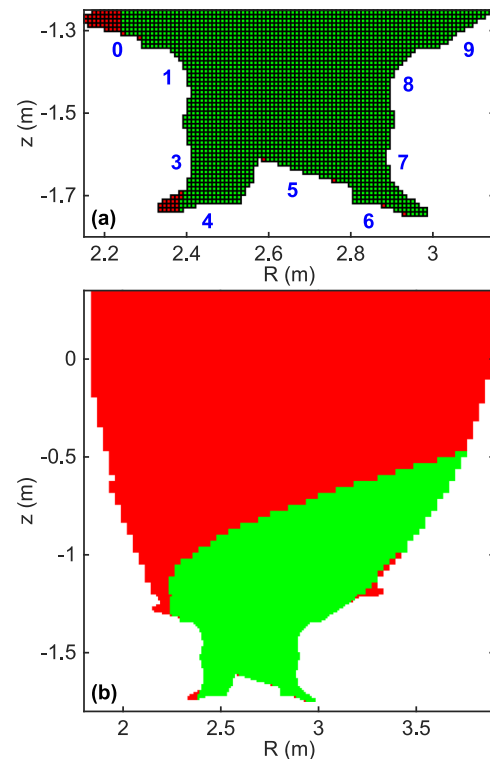


FIG. 3. The divertor volume is covered with grid cells of $1.0 \text{ cm} \times 1.0 \text{ cm}$ (a), and the grid is extended to the main chamber with cells of $3.0 \text{ cm} \times 3.0 \text{ cm}$ to account for the entire camera field-of-view (b). Tomographic reconstructions are generated in the green regions in (b), while the red regions are outside the field-of-view and ignored in the tomography process. The blue numbers in (a) label the different divertor tiles.

in Fig. 3(b), resulting in a total of 3486 active cells in the tomography calculations. Due to the reflections significantly increasing the density of nonzero elements in the geometry matrix, generating a reconstruction of a single camera frame lasts approximately 3–10 min, depending on the degree of binning applied on the 1000×1000 -pixel camera image.

III. RECONSTRUCTION BENCHMARKS WITH SYNTHETIC EMISSION

A set of four synthetic emission distributions, presented in Figs. 4(a)–4(d) were generated to investigate the effect and contribution of reflections on camera images and tomographic reconstructions. To provide a range of benchmark cases with emission and reflections in different parts of the divertor, emission patterns were created to extend from the divertor targets toward the X-point (XP) in vertical-horizontal (VH), corner-corner (CC), and vertical-vertical (VV) divertor configurations with inner and outer strike points on tiles 3 and 5, 4 and 6, and 3 and 7, respectively. The locations of the different divertor tiles are indicated in Fig. 3(a). Moreover, a fourth pattern was generated in the VH configuration with emission blobs placed on the high- and low-field sides (H/LFS) above the vertical level of the X-point (AXP) and detached

from the wall surfaces. Synthetic data was used to provide a well-defined reference for comparisons with the tomography solutions, as well as to restrict the observed effects to reflections only, eliminating, e.g., any remaining misalignment between an experimental camera view and the geometry calibration used for generating the geometry matrix. For this purpose, noise, which is always present in experimental data, was also omitted from the synthetic approach.

A. Contribution of reflections in camera images

The emission distributions in Figs. 4(a)–4(d) were multiplied with the reflection-corrected geometry matrix according to Eq. (1) to generate synthetic camera images presented in Figs. 4(e)–4(h). To distinguish reflected light in the images, synthetic camera images of the plasma emission only were generated similarly using a geometry matrix without the reflection correction and subtracted from the synthetic images in Figs. 4(e)–4(h). The resulting reflection contributions are presented in Figs. 4(i)–4(l).

In the brightest regions of the images, where the camera observes the plasma emission directly, reflections account for only up to 10% of the image. However, these regions are fairly narrow, while most of the divertor is illuminated in Figs. 4(e)–4(h) with

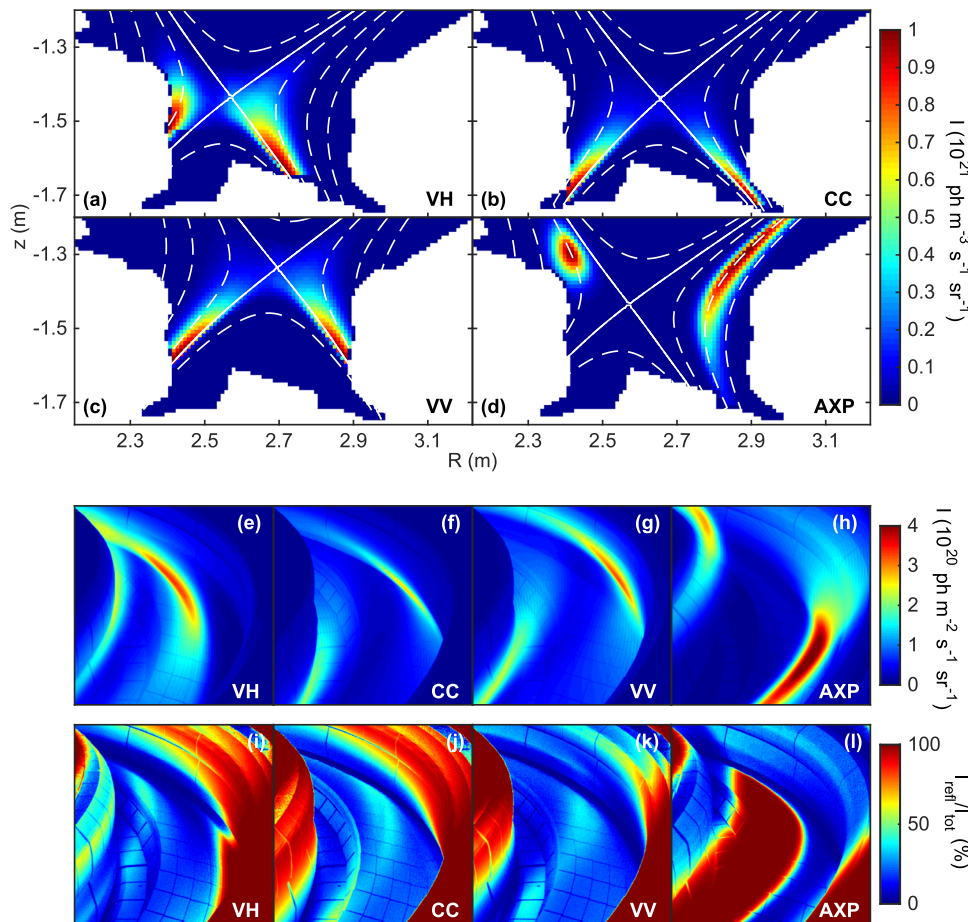


FIG. 4. Synthetic emission distributions were generated for benchmark purposes in vertical-horizontal (VH) (a), corner-corner (CC) (b), and vertical-vertical (VV) (c) configurations, as well as in VH configuration with emission above the vertical level of the X-point (AXP) (d), with synthetic camera images [(e)–(h)] created using the reflection-corrected geometry matrix and Eq. (1). Separation of the reflection contribution in the images [(i)–(l)] indicates amplification of the brightest regions by approximately 10%, while up to 50%–100% of the remote regions in the images are comprised of reflections.

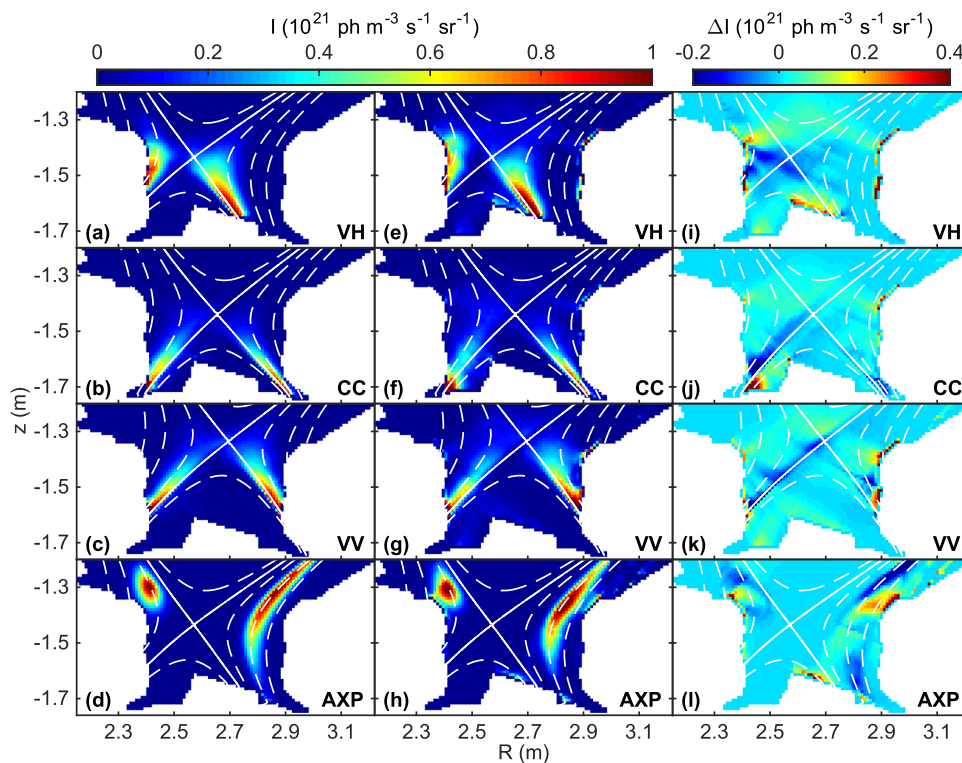


FIG. 5. Tomographic reconstructions of the synthetic images in Figs. 4(e)–4(h) with the reflection correction [(a)–(d)] reproduce the reference emission distributions in Figs. 4(a)–4(d) accurately within 2%–10%. Without the correction [(e)–(h)], localization of the emission is degraded and artifacts appear near wall surfaces, as also indicated by the difference between the uncorrected and corrected reconstructions [(i)–(l)].

visible tile features indicating reflections of the main emission. In regions remote from the main emission—such as tile 8 in the VH, CC, and VV configurations, tile 1 in the CC and VV configurations and tiles 4–5 in the AXP case—reflections can comprise up to 50%–100% of the image. Even in regions where reflections from wall surfaces are seen through the revolved main emission cloud, such as tile 5 in the VH and VV configurations and tiles 7–8 in the AXP case, reflections account for 25%–35% of the image. Interpreting these contributions in tomography as plasma emission can, thus, be expected to yield additional emission features near the wall surfaces in the reconstructions, setting need for the applied reflection correction.

B. Effect of reflections on tomographic reconstructions

To investigate the effect of reflected light being misinterpreted as plasma emission on tomography, tomographic reconstructions were generated from the synthetic images in Figs. 4(e)–4(h) using geometry matrices both with and without the reflection correction. With the correction, the reconstructions in Figs. 5(a)–5(d) reproduce the reference emission distributions in Figs. 4(a)–4(d) primarily within the accuracy of 2%–10%, benchmarking the functionality of the tomography algorithm with well-defined camera geometry calibration.

Without the correction in Figs. 5(e)–5(h), deviations from the reference emission distributions are observed. Spatial reproduction of the emission distributions is degraded, as the algorithm concentrates the emission closer to the wall surface in an attempt of

replicating the reflected light, as indicated by the differences between the reconstructions without and with the reflection correction in Figs. 5(i)–5(l). The effect is the most prominent near the inner target in VH and CC configurations, where neglecting the reflections pushes the emission blob toward tiles 1 and 4, respectively, and decreases it in the volume between the target and the X-point. In the former case, the emission is consequently spread wider along the target, while the emission pattern shifts from the scrape-off layer (SOL) partially to the private-flux region (PFR) in the latter.

The effect of misinterpreting the reflected light as plasma emission is, expectedly, the strongest near the wall surfaces. This is visualized in Fig. 6, where poloidal distributions of the emission along the edge of the reconstruction grid are compared between the reference emission distribution and the tomographic reconstructions with and without the reflection correction. As in Fig. 5, the emission along the edges of the reflection-corrected reconstructions primarily agrees closely with the references, the greatest deviation being a 15% overestimation of the HFS emission peak in the lower corner of the inner divertor between tiles 3 and 4 in Fig. 6(b). In the corner region, the tomography process is complicated by the restricted camera view, as indicated by the strong decrease of the weight of this region in the algorithm in Figs. 2(b) and 2(c).

The concentration of the emission near the wall surfaces observed in the 2D reconstructions without the reflection correction is seen in Fig. 6 as overestimation and spreading of the emission peaks. In the VH configuration in Figs. 5(e) and 6(a), the HFS peak emission is overestimated by up to 80% and emphasized further upwards along tile 1, when reflections are neglected, while

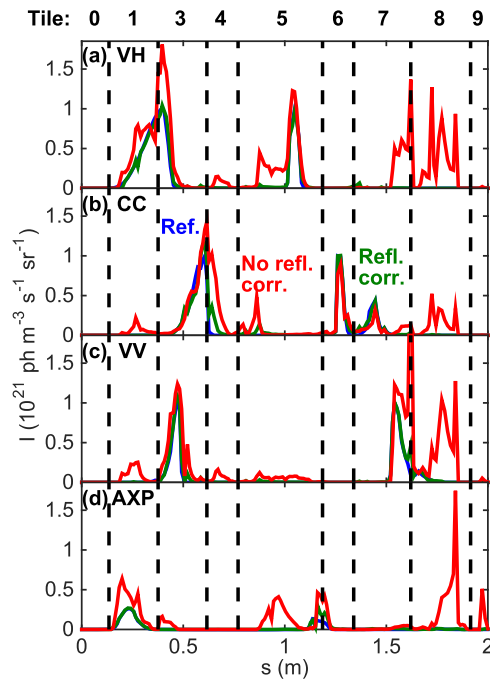


FIG. 6. Poloidal distributions of emission along the edges of the reconstruction grid in the VH (a), CC (b), VV (c) and AXP (d) configurations primarily indicate accurate reproduction of the reference emission (blue) by the reflection-corrected tomographic reconstructions (green), whereas overestimation and widening of the edge emission together with additional emission artifacts are observed without the reflection correction (red). The coordinate s increases poloidally along the edge of the reconstruction grid, starting on tile 0 on the top of the inner divertor. The vertical dashed lines indicate transitions between adjacent tiles, as indicated in Fig. 3(a).

overestimation of 20% is observed at the LFS peak on tile 5. In the CC configuration in Figs. 5(f) and 6(b), the peak emission at the inner strike point is overestimated by 40%, and misinterpretation of reflected light from tile 4 gives rise to strong emission in the PFR with comparable intensity to the reference emission in the SOL. In the VV configuration in Figs. 5(g) and 6(c), the HFS peak on tile 3 is widened in both directions with a 25% overestimation of the maximum intensity, while the LFS peak on tile 7 is spread substantially upwards towards tile 8. While the brightest parts of emission in the AXP case in Figs. 5(h) and 6(d) are not similarly in contact with the wall surfaces as in the other configurations, misinterpretation of the illuminated surface tends to bridge the gap between the emission blob and the wall, leading to overestimation of the edge emission by up to a factor of 4.

In addition to the degraded localization of the main emission regions, a prominent feature in the uncorrected tomographic reconstructions in Figs. 5 and 6 is the appearance of emission artifacts at the wall surfaces. This is especially the case in front of tile 5 in the VH and AXP configurations and at tiles 7 and 8 in the outer divertor in all cases. As less localized and intense artifacts, also background halos appear above the X-point and in the inner divertor leg. Similar observations were made also in Refs. 22 and 23.

IV. CONTRIBUTION OF REFLECTIONS IN ANALYSIS OF EXPERIMENTAL CAMERA DATA

The effect of reflections on tomographic reconstructions of experimental camera images was assessed during a JET L-mode n_e ramp pulse no. 90415 at different stages of outer divertor detachment. The Balmer D_α emission, recorded using a narrow-pass filter with a central wavelength of 656.1 nm and bandwidth of 1.5 nm, was investigated at three different LFS edge densities above the detachment roll-over density of $n_{e,edge,LFS}^{roll-over} \approx 2.8 \times 10^{19} \text{ m}^{-3}$, providing qualitatively and quantitatively different divertor emission properties with noticeable presence of reflections from especially tile 5, as shown in the camera images in Figs. 7(a)–7(c).

The reflection-corrected tomographic reconstructions in Figs. 7(d)–7(f) show extension of the LFS D_α emission from the outer strike point on tile 5 towards the X-point with increasing $n_{e,edge,LFS}$, while the HFS emission is less bright and concentrated in front of the inner target. Immediately above the roll-over density, at $n_{e,edge,LFS} = 3.0 \times 10^{19} \text{ m}^{-3}$ in Fig. 7(d), the LFS emission is concentrated in the vicinity of the outer strike point, while at $n_{e,edge,LFS} = 4.0 \times 10^{19} \text{ m}^{-3}$ in Fig. 7(e), the emission cloud is brighter and more elongated, reaching halfway to the X-point. At the highest density of $n_{e,edge,LFS} = 4.8 \times 10^{19} \text{ m}^{-3}$ in Fig. 7(f), the LFS emission forms a uniform plume which extends from the strike point to above the X-point. The evolution of the emission intensity with increasing $n_{e,edge,LFS}$, indicating the rate of the extension, is illustrated in Fig. 8(b) in three locations along the emission plume, marked with purple crosses in Fig. 8(a).

Without the reflection correction, the reconstructions in Figs. 7(g)–7(i) show similar behavior with respect to the reflection-corrected reconstructions as discussed in Sec. III B. As highlighted by the subtractions between the uncorrected and corrected reconstructions in Figs. 7(j)–7(l), the most notable difference is the appearance of an approximately 5 cm thick emission artefact along the surface of tile 5 between the outer strike point and the HFS edge of the tile. This is a symptom of misinterpretation of the reflections on tile 5 seen clearly in Figs. 7(b) and 7(c), as the extending emission cloud illuminates the tile from above.

Near the surface of tile 5, reflections are observed to amplify the main emission region at the outer strike point by 15%–20% independent of the brightness of the emission. This is presented in Fig. 9 which presents the emission intensity and the relative contribution of reflections in it as functions of the vertical distance from the tile 5 surface at the three radial positions indicated by purple dashed lines in Fig. 8(a). While Figs. 9(a) and 9(b) concentrate on the highest density of $n_{e,edge,LFS} = 4.8 \times 10^{19} \text{ m}^{-3}$, Figs. 9(c)–9(e) cover the evolution of the emission intensity over the entire density range. Interpreting reflections as part of the emission distribution is, expectedly, seen to amplify the emission, and Fig. 9(c) suggests that this amplification is fairly constant, when the emission takes place in the vicinity of the wall surface. When the emission cloud illuminates tile 5 from a longer distance above the tile surface, Figs. 9(d) and 9(e) show an increase of the reflection contribution near the surface to up to 50%. Unlike at the strike point in Fig. 9(c), the reflection contribution can be seen to increase with emission intensity especially at the LFS end of tile 5 in Fig. 9(e), suggesting that the interpreted emission in the PFR is primarily reflected light from the emission cloud. Instead, at the actual emission peak positions 7–15 cm above tile 5,

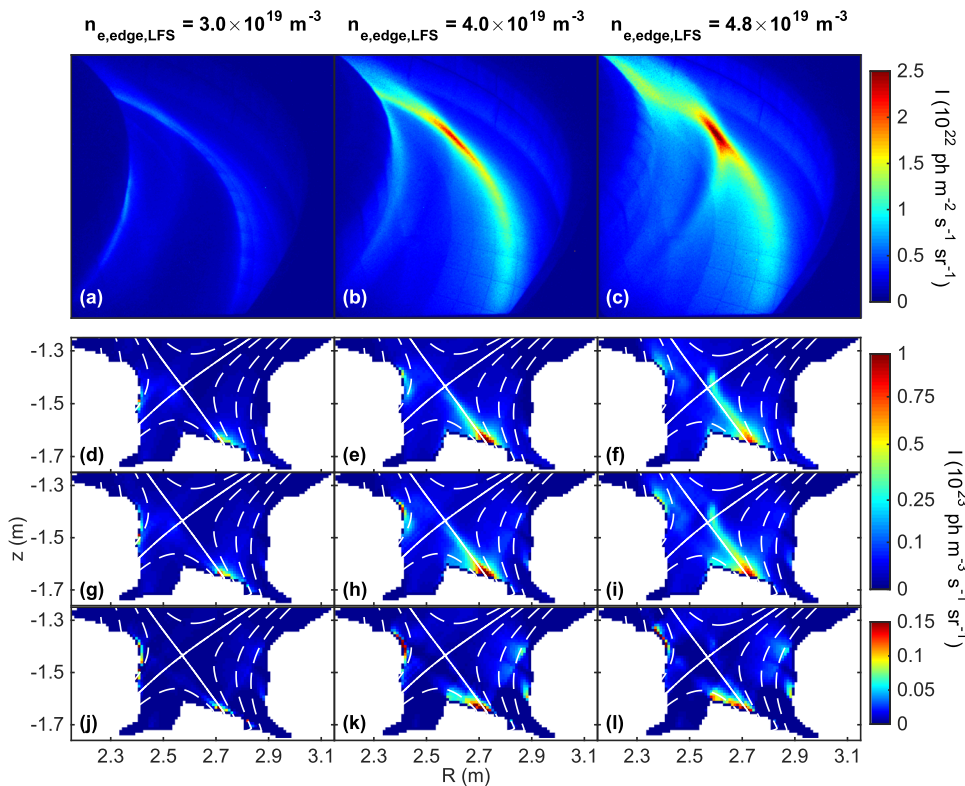


FIG. 7. Tomographic reconstructions of experimental camera images of D_α emission [(a)–(c)] with the reflection correction show extension of the LFS emission from outer strike point towards the X-point with increasing $n_{e,\text{edge,LFS}}$ [(d)–(f)]. Uncorrected reconstructions [(g)–(i)], as well as the subtractions between uncorrected and corrected reconstructions [(j)–(l)] indicate appearance of a bright emission artefact in front of tile 5 due to misinterpreted reflected light. Note the nonlinear color bar in (d)–(i).

the amplification falls to below 10% due to the increasing distance to the reflecting surface.

It is noted that the geometry calibration used for generating the geometry matrix is not perfectly aligned with the camera view

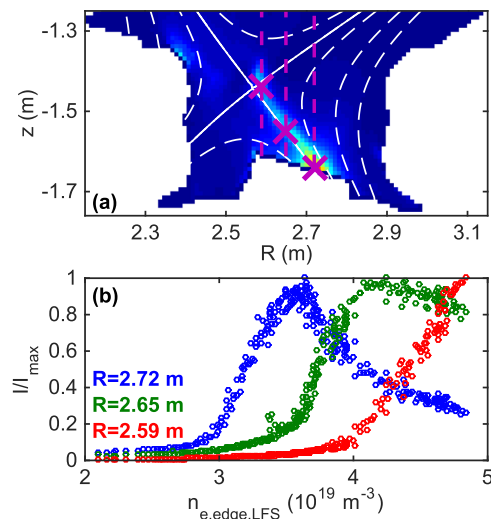


FIG. 8. Normalized emission intensities at three radial positions along the LFS emission pattern, marked with purple crosses in (a), show the extension of the emission from the outer strike point to the X-point with increasing $n_{e,\text{edge,LFS}}$ (b).

during pulse no. 90415. While the mechanical setup of the divertor camera system is fairly robust, the cameras have been observed to move, e.g., during disruptions. In addition, the optical properties of different applied wavelength and neutral density filters may slightly change the view. As a result, the correspondence between the camera view and the geometry calibration should ideally be confirmed for each pulse for which tomography is applied to optimize the validity of Eq. (1). The reconstructions in Fig. 7 may thus still contain some emission artifacts due to the remaining misalignment. As part of the development process of camera tomography in JET, a tool for correcting the camera view with respect to a well-defined reference calibration is being constructed. This is expected to further decrease the emission artifacts and to make the reconstructions more steadily reliable without a need for repeating the computationally heavy process of regenerating the geometry matrix for every pulse.

V. CONTRIBUTION OF REFLECTIONS IN THE DIVERTOR SPECTROSCOPY

In addition to camera images, reflections from wall surfaces interfere also with line-integrated spectroscopic measurements in the divertor. To investigate the magnitude of this effect, divertor spectroscopy was mimicked by integrating the tomographic reconstructions discussed in Sec. IV along lines-of-sight of the vertical divertor spectroscopy setup of JET,⁸ presented in Fig. 10(a). Due to lack of information of the 2D distributions of the divertor plasma parameters in the experimental cases, such an investigation could,

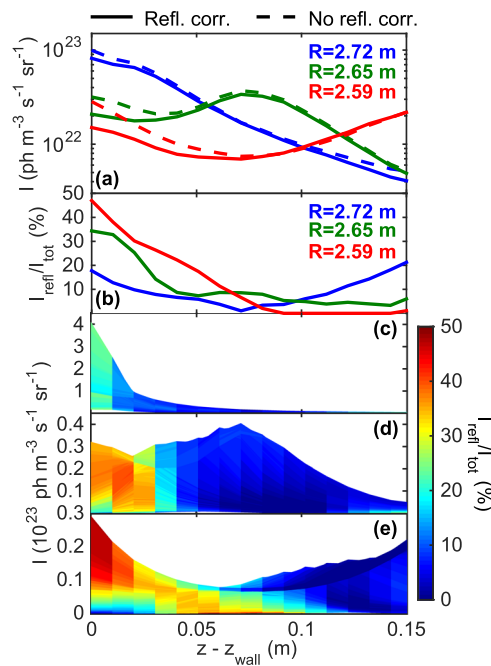


FIG. 9. Comparison of emission intensities (a) with (solid) and without (dashed) the reflection correction as a function of vertical distance from tile 5 surface along the magenta dashed lines in Fig. 8(a) shows approximately 20% amplification of emission near outer strike point due to reflections and up to 50% reflection contributions at the HFS edge of tile 5 (b). Investigation of the reflection contribution as a function of the emission intensity suggests no intensity dependence on reflection amplification at the outer strike point (c), whereas the contribution of reflections becomes more significant with increasing intensity, when the tile is illuminated from further above the surface (d) and (e). Note the logarithmic scale in (a).

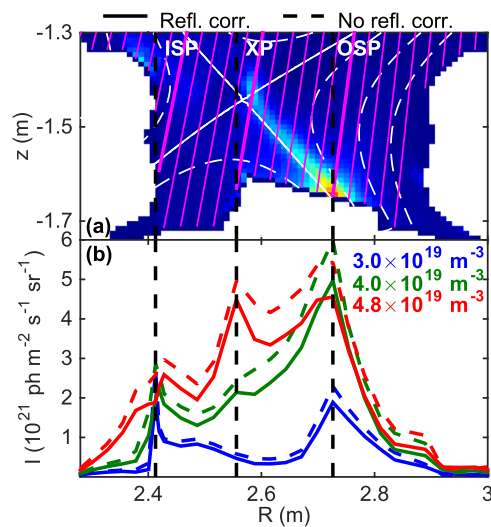


FIG. 10. Divertor spectroscopy measurements are mimicked by integrating the tomographic reconstructions along the KT1 lines-of-sight (a), showing amplification of the emission peaks at the strike points by 15%–25% between reflection-corrected (solid) and uncorrected (dashed) profiles (b). The black vertical dashed lines indicate the radial positions of the inner and outer strike points (I/OSP) and the X-point (XP).

however, only be done for the spectroscopically measured line intensities. Therefore, to study the effect of reflections on spectroscopic measurements of divertor n_e and T_e , the CHERAB code with reflections considered by ray-tracing^{34,35} was used to generate synthetic 3D emission patterns from solutions of EDGE2D-EIRENE simulations which were further postprocessed with synthetic spectroscopy to replicate the n_e and T_e measurements.³⁶

A. Amplification of spectroscopy signal by reflections

The contributions of reflections in the 2D emission distributions in Fig. 7 are observed to amplify the peaks of the line-integrated emission profiles at the strike points by 15%–25% throughout the density range, as indicated by the profiles in Figs. 10(b) and 11(b). The extension of the emission pattern toward the X-point is seen in the line-integrated data in Fig. 11(a) as gradual brightening of the region between the outer strike point and the X-point, followed by the magenta dashed line, culminating in the formation of an additional emission peak in the emission profile at the X-point at the highest density in Fig. 10(b).

The extension of the emission region coincides with a decrease in the contribution of reflections between the outer strike point and the X-point from 25%–35% to 15%–25% in Fig. 11(b). The decrease is in contrast with the significantly increased reflection contributions observed locally in the 2D reconstructions at high densities in Figs. 7 and 9. This is due to the line-integrated spectroscopic measurement being dominated by the most intense emission along the line-of-sight. As discussed in Sec. IV, the amplification of the main emission region due to reflections between the outer strike point and the X-point is only of the order of 10%. Since the spectroscopic lines-of-sight pass through the emission cloud, the strong local effects

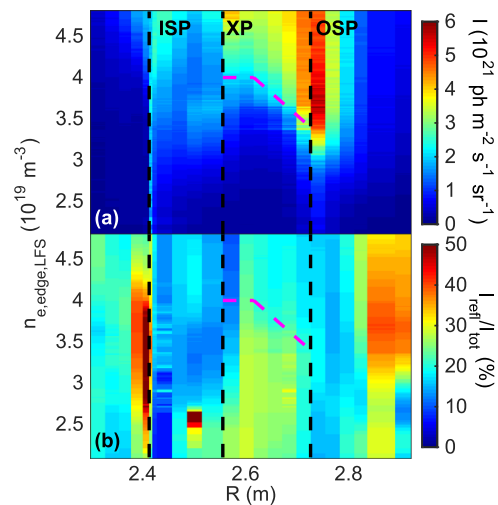


FIG. 11. The extension of the emission region is seen in the line integrals of the tomographic reconstructions as gradual brightening of the region between the outer strike point and the X-point (a), which coincides with a decrease of the reflection contribution from 25%–35% to 15%–25% (b), indicating dominance of the main emission in the spectroscopic signal. The magenta dashed line marks the edge of the extension of the emission pattern with increasing $n_{e,edge,LFS}$. The black vertical dashed lines indicate the radial positions of the inner and outer strike points (I/OSP) and the X-point (XP).

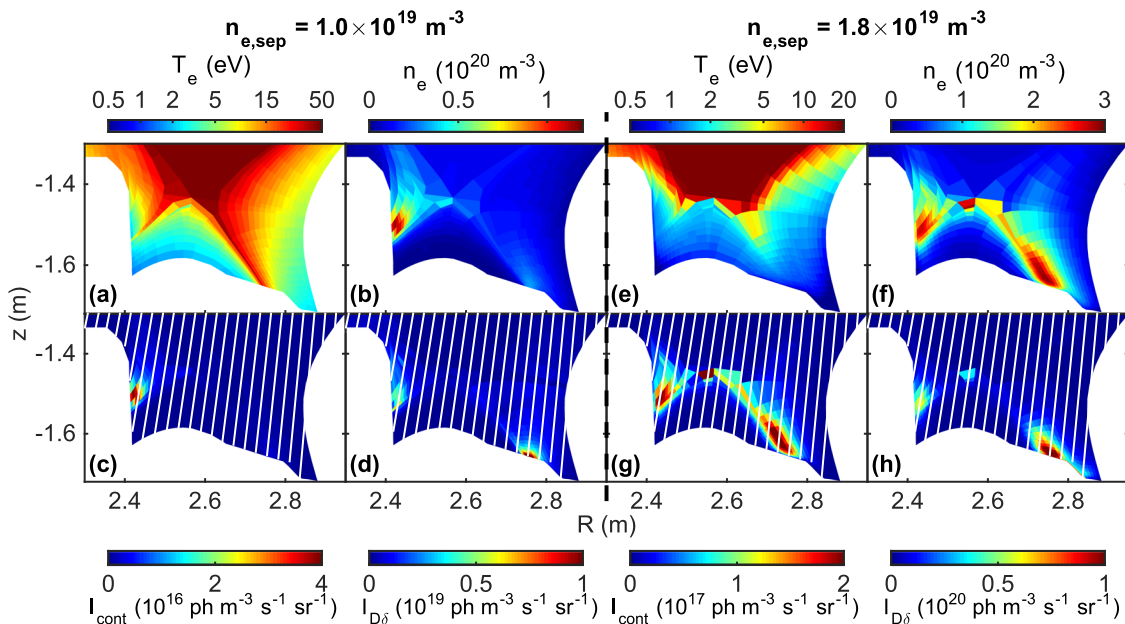


FIG. 12. 2D distributions of continuum emission [(c) and (g)] coincide with decreases in the divertor T_e [(a) and (e)], while the strongest Balmer D_δ emission [(d) and (h)] is observed in the regions of the highest divertor n_e [(b) and (f)] in postprocessed EDGE2D-EIRENE simulations at LFS separatrix densities of $n_{e,sep} = 1.0 \times 10^{19} \text{ m}^{-3}$ [(a)–(d)] and $n_{e,sep} = 1.8 \times 10^{19} \text{ m}^{-3}$ [(e)–(h)]. The spectroscopic lines-of-sight are indicated by the white lines on the emission maps [(c), (d), (g), and (h)]. Note the logarithmic color scales in (a) and (e) and the different color scales in the corresponding plots between (a)–(d) and (e)–(h). The color scales in the T_e maps [(a) and (e)] have been deliberately saturated in the core region for improved presentation of the divertor SOL and PFR conditions.

at the target are effectively shadowed, and less pronounced spatial variation in the reflection contribution is observed than in the 2D reconstructions.

B. Effect of reflections on spectroscopic n_e and T_e measurements

The effect of reflections on synthesized spectroscopic n_e and T_e measurements was investigated by postprocessing two EDGE2D-EIRENE simulations with LFS midplane separatrix densities of $n_{e,sep} = 1.0 \times 10^{19} \text{ m}^{-3}$ and $n_{e,sep} = 1.8 \times 10^{19} \text{ m}^{-3}$ and input power of 2.2 MW. The selected cases represent high-recycling conditions with variance in divertor n_e and T_e , as seen in Figs. 12(a), 12(b), 12(e), and 12(f).

Accounting for reflections in CHERAB is observed to decrease the synthetically inferred divertor T_e in Fig. 13(a), derived from the spectral shape of continuum emission, by 20%–50% between the strike points and by up to 75% in the remote regions near the upper corners of the divertor. This points at redistribution of the continuum emission in the brightest regions due to reflections having a considerable contribution in the observations in regions of weaker emission. Since the continuum emission is dominated by radiative recombination, the brightest emission originates from regions of low temperature, leading to the observed decrease in T_e in comparison to the no-reflections case.

Bright continuum emission is observed only at the inner strike point at $n_{e,sep} = 1.0 \times 10^{19} \text{ m}^{-3}$ in Fig. 12(c), coinciding with a

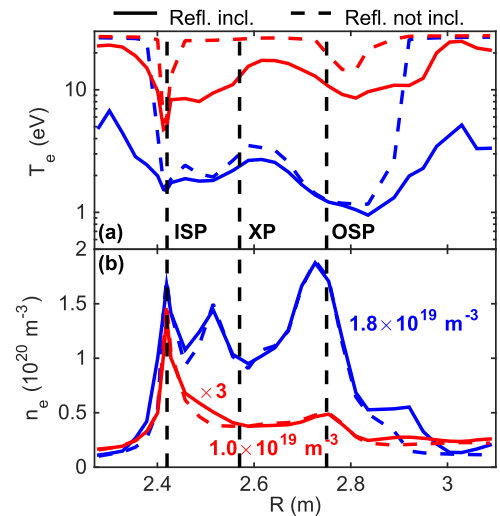


FIG. 13. Decrease of 20%–50% between the strike points and up to 75% in remote regions is observed, when reflections are considered in synthesized spectroscopic measurements of the divertor T_e (a), while no significant effect is observed in divertor n_e measurements (b). The black vertical dashed lines indicate the radial positions of the inner and outer strike points (I/OSP) and the X-point (XP). For illustrative purposes, the n_e curves for the $n_{e,sep} = 1.0 \times 10^{19} \text{ m}^{-3}$ case have been multiplied by a factor of 3 in (b) for improved indication of the difference between the solid and the dashes curve. Note the logarithmic scale in (a).

decrease in the inner divertor T_e in Fig. 12(a). In this region, the temperatures inferred with and without reflections agree in Fig. 13(a). Elsewhere in the divertor, reflections of this bright emission are sufficiently strong to dominate the line-integrated observations over the 1–2 orders of magnitude weaker continuum emission and, consequently, to decrease the inferred T_e in the regions of weaker emission. At $n_{e,\text{sep}} = 1.8 \times 10^{19} \text{ m}^{-3}$, the continuum emission forms elongated patterns between the strike points and the X-point, which dominate the spectroscopic signal between the strike points, leading to less significant decrease in the inferred T_e between the strike points. Near the upper corners of the divertor, however, reflections from the strike-point regions have a more pronounced role, leading to the observed 75% decrease in T_e in Fig. 13(a).

In the case of divertor n_e , derived from the Stark broadening of the Balmer D_δ line, the synthetic measurements do not show as significant differences due to reflections as for T_e at either of the upstream densities in Fig. 13(b). Since in a pure D plasma the D_δ emission scales with n_e^2 , reflections from the brightest emission regions are expected to increase the inferred divertor n_e . However, between the strike points, such an effect is observed only in the inner divertor as a 15%–30% increase in both $n_{e,\text{sep}}$ cases. Only near the upper corner of the outer divertor at $n_{e,\text{sep}} = 1.8 \times 10^{19} \text{ m}^{-3}$, the inferred n_e is strongly increased by up to a factor of 2.5 due to reflected light spreading into low-intensity regions of the divertor.

The lack of an effect between the outer strike point and the X-point can partially be attributed to the shallower poloidal n_e gradient in comparison to the inner divertor, which reduces the effect of reflections from the outer strike point to amplification of the emission intensity without a major effect on the line width from which n_e is inferred. Moreover, as discussed in Ref. 37, the width of the observed spectral line is less sensitive to the sum of the plasma emission with the reflection contribution than the more additive height of the recombination edge of the continuum spectrum, used for deriving the divertor T_e , which further explains the weaker effect of reflections in comparison to the T_e measurement.

VI. CONCLUSIONS

The contribution of reflections from metallic wall surfaces has been integrated into the geometry definition of tomographic reconstructions of the tangentially viewing, filtered visible-range spectroscopic divertor camera diagnostics of JET. The reconstructions thus present only the plasma emission without misinterpreted reflected light, which improves the localization of the emission and removes artifacts from the reconstructions.

Benchmarks with synthetic emission distributions suggest that reflections amplify the brightest regions in the divertor camera images by approximately 10%, while up to 50%–100% of the remote parts of the images are comprised of reflections. Misinterpreting these contributions as plasma emission was observed to give rise to bright emission artifacts in front of the wall surface and to overestimate the emission at the edges of the reconstruction grid by up to a factor of 4. Analysis of experimental camera data during and L-mode n_e ramp showed almost constant amplification of emission at the outer strike point by approximately 20% due to reflections, while the reflection correction was found to mitigate the formation of an increasingly bright artifact in front of tile 5, which comprised up

to 50% of the local emission without the correction, when the LFS emission pattern extends from the strike point toward the X-point.

Mimicking divertor spectroscopy measurements by line integration of the tomographic reconstructions showed amplification of the emission peaks at the strike points by 15%–25% due to reflections. Due to the dominance of the brightest emission observed along the spectroscopic lines-of-sight, the effect of reflections on the spectroscopy signal was found to be generally less pronounced than the local effects observed in the 2D reconstructions. However, postprocessing of EDGE2D-EIRENE simulations suggested a significant decrease of the spectroscopically inferred divertor T_e by up to 75% due to reflection-induced redistribution of the continuum emission from low- T_e regions. A similar effect was not observed in the case of n_e measurements due to the less pronounced variation in n_e between the brightest D_δ emission regions at the strike points and the weaker emission at the X-point, as well as due to the weaker sensitivity of the spectral line width to the addition of the reflective component.

While tomographic reconstructions based on the camera viewing geometry alone provide an adequate description of the 2D emission characteristics in the JET divertor, the improved localization and removal of emission artifacts through the introduction of the reflection correction is found to improve the quality and representativity of the reconstructions. Consequently, the comparability between the camera data and divertor modeling is improved with less emission features left open for interpretation. Further improvement is being pursued by on-going development of spatial variation in the reflection model and alignment correction for the camera images. It is also noted that in analysis of spectroscopic measurements, the role of reflections is not restricted to amplification of the recorded signal, but the redistribution of the observed light can have a significant effect on inference of the divertor plasma parameters.

ACKNOWLEDGMENTS

This work has been carried out within the framework of the EUROfusion Consortium and has received funding from the Euratom research and training programme 2014–2018 and 2019–2020 under grant agreement No. 633053. The views and opinions expressed herein do not necessarily reflect those of the European Commission.

REFERENCES

- ¹G. P. Maddison *et al.*, *Nucl. Fusion* **43**, 49–62 (2003).
- ²A. Kallenbach *et al.*, *Plasma Phys. Controlled Fusion* **55**, 124041 (2013).
- ³M. Bernert *et al.*, *Nucl. Mater. Energy* **12**, 111–118 (2017).
- ⁴D. Lumma, J. L. Terry, and B. Lipschultz, *Phys. Plasmas* **4**, 2555 (1997).
- ⁵S. Potzel, R. Dux, H. W. Müller, M. Wischmeier, and ASDEX Upgrade Team, *Plasma Phys. Controlled Fusion* **56**, 025010 (2014).
- ⁶B. A. Lomanowski, A. G. Meigs, R. M. Sharples, M. Stamp, C. Guillemat, and JET Contributors, *Nucl. Fusion* **55**, 123028 (2015).
- ⁷A. Huber *et al.*, *Fusion Eng. Des.* **82**, 1327–1334 (2007).
- ⁸K. D. Lawson *et al.*, *Rev. Sci. Instrum.* **83**, 10D536 (2012).
- ⁹A. G. Meigs, M. Stamp, R. Igraja, S. Sanders, P. Heesterman, and JET-EFDA Contributors, *Rev. Sci. Instrum.* **81**, 10E532 (2010).
- ¹⁰B. A. Lomanowski, A. G. Meigs, N. J. Conway, K.-D. Zastrow, R. M. Sharples, P. Heesterman, D. Kinna, and JET EFDA Contributors, *Rev. Sci. Instrum.* **85**, 11E432 (2014).

- ¹¹A. Huber *et al.*, *Rev. Sci. Instrum.* **83**, 10D511 (2012).
- ¹²T. M. Biewer, C. Belcher, I. Hassall, D. L. Hillis, G. Kaveney, D. Scharpf, M. F. Stamp, C. Stunell, K.-D. Zastrow, and JET-EFDA Contributors, *Rev. Sci. Instrum.* **83**, 10D505 (2012).
- ¹³V. Huber *et al.*, *Rev. Sci. Instrum.* **87**, 11D430 (2016).
- ¹⁴N. J. Conway, A. J. Cackett, C. F. Maggi, A. G. Meigs, K.-D. Zastrow, T. M. Biewer, and D. L. Hillis, *Rev. Sci. Instrum.* **89**, 10K107 (2018).
- ¹⁵M. E. Fenstermacher, W. H. Meyer, R. D. Wood, D. G. Nilson, R. Ellis, and N. H. Brooks, *Rev. Sci. Instrum.* **68**, 974 (1997).
- ¹⁶M. E. Fenstermacher *et al.*, *J. Nucl. Mater.* **241-243**, 666–671 (1997).
- ¹⁷M. E. Fenstermacher *et al.*, *J. Nucl. Mater.* **266-269**, 348–353 (1999).
- ¹⁸C. J. Boswell, J. L. Terry, B. Lipschultz, and J. Stillerman, *Rev. Sci. Instrum.* **72**, 935 (2001).
- ¹⁹B. P. Duval, J.-M. Moret, and R. A. Pitts, *Bull. Am. Phys. Soc.* **44**, GP175 (1999).
- ²⁰K. Itami, P. Coad, W. Fundamenski, C. Ingesson, J. Lingertat, G. F. Matthews, and A. Tabasso, *J. Nucl. Mater.* **290-293**, 633–638 (2001).
- ²¹A. Huber *et al.*, *J. Nucl. Mater.* **313-316**, 925–930 (2003).
- ²²J. Harhausen, A. Kallenbach, C. Fuchs, and ASDEX Upgrade Team, *Plasma Phys. Controlled Fusion* **53**, 025002 (2011).
- ²³M. Odstrčil, J. Mlynář, V. Weinzettl, P. Háček, T. Odstrčil, G. Verdoolaege, M. Berta, T. Szabolics, and A. Bencze, *Rev. Sci. Instrum.* **85**, 013509 (2014).
- ²⁴J. R. Harrison, S. W. Lisgo, K. J. Gibson, P. Tamain, J. Dowling, and MAST Team, *J. Nucl. Mater.* **415**, S379–S382 (2011).
- ²⁵A. Huber *et al.*, *J. Nucl. Mater.* **438**, S139–S147 (2013).
- ²⁶G. F. Matthews *et al.*, *Phys. Scr.* **T145**, 014001 (2011).
- ²⁷M. Carr *et al.*, *Rev. Sci. Instrum.* **90**, 043504 (2019).
- ²⁸R. Simonini, G. Corrigan, G. Radford, J. Spence, and A. Taroni, *Contrib. Plasma Phys.* **34**, 368 (1994).
- ²⁹D. Reiter, *J. Nucl. Mater.* **196-198**, 80–89 (1992).
- ³⁰S. Wiesen, “EDGE2D/EIRENE code interface report,” JET ITC-Report, 2006, www.eirene.de/e2deir_report_40jun06.pdf.
- ³¹J. Roth *et al.*, *Plasma Phys. Controlled Fusion* **50**, 103001 (2008).
- ³²A. H. Andersen and A. C. Kak, *Ultrason. Imaging* **6**, 81–94 (1984).
- ³³W. Lu and F.-F. Yin, *Med. Phys.* **31**, 3222–3230 (2004).
- ³⁴C. Giroud, A. Meakins, M. Carr, A. Baciero, and C. Bertrand (2018). “CHERAB spectroscopy modelling framework (version v0.1.0),” Zenodo. <http://doi.org/10.5281/zenodo.1206142>.
- ³⁵M. Carr *et al.*, in 44th EPS Conference on Plasma Physics, 2017, O5.130.
- ³⁶B. A. Lomanowski *et al.*, *Nucl. Mater. Energy* **20**, 100676 (2019).
- ³⁷B. A. Lomanowski, M. Groth, I. Coffey, J. Karhunen, C. F. Maggi, A. G. Meigs, S. Menmuir, M. O’Mullane, and JET Contributors, “Interpretation of Lyman opacity measurements in JET with the ITER-like wall using a particle balance approach,” *Plasma Phys. Controlled Fusion* (submitted).